Rare Met.
https://doi.org/10.1007/s12598-024-03071-3

RARE METALS

ORIGINAL ARTICLE

All-fiber anti-jamming capacitive pressure sensors based on liquid metals

Hui-Chen Xu, Yue Liu, Ye-Pei Mo, Zi-Yu Chen, Xiao-Jun Pan, Rong-Rong Bao*, Cao-Feng Pan*

Received: 27 May 2024 / Revised: 5 July 2024 / Accepted: 11 July 2024

Abstract Capacitive pressure sensors have a promising application in the field of wearable electronic devices due to their excellent electrical properties. Owing to the complexity of the environment, capacitive sensors are susceptible to electromagnetic interference and changes in the surrounding medium, resulting in unstable signal acquisition. Capacitive sensor with excellent immunity to interference while maintaining flexibility is an urgent challenge. This study proposes an all-fiber anti-jamming capacitive pressure sensor that integrates liquid metal (LM) into a fiber-based dielectric layer. The combination of the LM and the fiber not only improves the dielectric properties of the dielectric layer but also reduces the Young's modulus of the fiber. The sensor has high interference immunity in various noise environments. Its all-fiber structure ensures lightweight, great air permeability and stretchability, which makes it a promising application in wearable electronic devices fields.

Keywords Liquid metal; Anti-jamming; Pressure sensors; Dielectric properties; Hybrid electrospinning

1 Introduction

Flexible tactile sensors play an indispensable role in human–computer interaction [1–9], electronic skin [10–19], robotics and other fields [20–24]. Among them, flexible capacitive pressure sensors are widely employed for pressure, displacement, vibration and other measurements due to their simple structure, high resolution, good dynamic response and easy processing [25–32]. Typically, a capacitive sensor consists of top and bottom electrodes, an insulator and a substrate [33]. When pressure is applied, the film deforms, altering the capacitance by varying the distance between the electrodes [34, 35]. However, capacitive sensors are susceptible to external disturbances that can cause their performance to become unstable [36–38]. Therefore, there is an urgent need to develop a flexible capacitive pressure sensor with anti-jamming capability.

Recent research has focused on doping flexible matrix materials with conductive particles or inorganic nanoparticles to enhance their electrical properties [39–41]. These studies have demonstrated novel properties of flexible sensors in terms of high-temperature resistance [42, 43], implantability [44, 45], electromagnetic shielding [46, 47] and negative dielectric constant modulation [48–50], which have potential applications [51, 52]. For example, Pan's group proposed a flexible pressure sensor with high anti-jamming capacitance using polyvinylidene fluoride

Supplementary Information The online version contains supplementary material available at https://doi.org/10.1007/s12598-024-03071-3.

H.-C. Xu, Z.-Y. Chen, X.-J. Pan, C.-F. Pan*
Center On Nanoenergy Research, Institute of Science and Technology for Carbon Peak and Neutrality, Key Laboratory of Blue Energy and Systems Integration, Education Department of Guangxi Zhuang Autonomous Region, School of Physical Science and Technology, Guangxi University, Nanning 530004, China
e-mail: pancaofeng@buaa.edu.cn

H.-C. Xu, Y. Liu, Y.-P. Mo, Z.-Y. Chen, R.-R. Bao*, C.-F. Pan
Beijing Institute of Nanoenergy and Nanosystems, Chinese Academy of Sciences, Beijing 101400, China
e-mail: baorongrong@buaa.edu.cn

C.-F. Pan
Institute of Atomic Manufacturing, Beihang University, Beijing 100191, China

Published online: 27 March 2025

(PVDF)@silver nanowires (Ag NWs)@TiO_2 film as the dielectric layer [53]. Similarly, Song's group improved anti-jamming performance by co-assembling $Ti_3C_2T_x$ (MXene) and cellulose nanofibers via a freeze-drying process, followed by surface encapsulation with flame-retardant thermoplastic polyurethane (TPU) to fabricate MXene composite gels [54]. Xu et al. [55] developed a composite film incorporating reduced graphene oxide (rGO) and polyacrylic acid (PAA) for electromagnetic interference (EMI) shielding application. These innovations offer promising pathways for the development of capacitive flexible pressure sensors with high immunity to interference.

However, the integration of highly doped inorganic components can significantly diminish the flexibility of the matrix materials. As novel materials, liquid metal (LM) exhibits both the fluidity of liquids and the conductivity of metals [56–61]. Research has demonstrated that the incorporation of inorganic particles elevates Young's modulus of elastomers, whereas the inclusion of LM does not [62, 63]. The internal LM particles maintain their integrity under stress, thereby improving the dielectric constant and capacitance properties of the composites [64–66]. Therefore, replacing traditional inorganic functional nanoparticles with LM can effectively realize the construction of soft elastomer devices with high sensitivity, dielectric constant and composite [67].

Electrospinning has emerged over the last few years as a key technology for versatile, feasible and low-cost manufacturing of wearable devices [68–74]. Since wearable electronic devices are mostly in contact with the human body, textiles are preferred for daily and long-term use due to their flexibility, fineness, breathability and heat dissipation. Textiles offer excellent stretchability, large surface area and high porosity, making them ideal for embedding electronic materials without compromising softness [75]. Herein, we have developed an all-fiber anti-jamming capacitive pressure sensor modified with LM for human health monitoring. The sensor employs a hybrid electrospinning technique to fabricate a fiber-based dielectric layer incorporating modified LM particles and TPU elastomers. Blending the flexible matrix material with the LM improves the electrical properties of the dielectric layer and endows the device with excellent anti-jamming capability. Finally, the all-fiber-based device effectively reduces Young's modulus of each functional layer and improves its tensile deformation capability. The signal-to-noise ratio (SNR) of this sensor is nearly three times higher than that of the pure TPU fiber dielectric layer-integrated sensor under various electromagnetic interferences. This indicates that the device has a higher resistance to interference. The low Young's modulus and high elongation at break through the dielectric layer give the sensor a broad detection range of 2100 kPa. It maintains stability and repeatability under more than 20,000 loading–unloading cycles in a noisy environment. In addition, it can monitor physiological parameters such as respiration and movement, which is crucial for the timely detection of health abnormalities and intervention. It holds significant promise for future applications in healthcare, enabling new possibilities for personalized and continuous health monitoring.

2 Experimental

2.1 Materials

TPU pellets (75 A) were purchased from Shanghai Baijinrun Plastic Material Co., Ltd. N,N-dimethylformamide (DMF, 99.9%) and tetrahydrofuran (THF, 99%) were purchased from Beijing Essun Huitong Technology Co., Ltd. LM (EGaIn, Melting point: 16 °C) was purchased from Dongguan Huatai Metal Materials Technology Co., Ltd. Poly(sodium 4-styrenesulfonate) (PSS, *M*w 1,000,000) was purchased from Shanghai Yuanchun Biotechnology Co., Ltd. Acetic acid (AA, 99%), Ag and carbon black powder were purchased from Aladdin. Ag nanowires (Ag NWs, 5 mg·mL^{-1} in DMF) were purchased from Guangzhou Blueglownano Materials. All of the materials were used as received without further purification.

2.2 Preparation of LM-modified ink-1

Firstly, 1 g EGaIn (bulk LM) was added to dilute AA (5 vol%, 3 mL). To achieve uniform dispersion of LM, different masses of PSS (0.006, 0.01, 0.014, 0.018 and 0.022 g) were added to the LM-AA solution. The composite solution was sonicated (VC 505, 3 mm microtip, pulse on 10 s and pulse off 10 s) at 500 W and 20 kHz for 40 min. The modified ink is referred to as PaLMP ink-1.

2.3 Preparation of TPU electrospinning solution

Firstly, DMF and THF (mass ratio 1:1) were dropped into a screw-top vial and TPU pellets were added. Next, the solution was stirred thoroughly for 4 h (70 °C, 1,500 r·min^{-1}). Finally, the TPU electrospinning solution (15 wt%) was obtained.

2.4 Preparation of hybrid inks for TPU with LM (TPU @LM ink-2)

0.005 g PSS was added to the TPU (15 wt%) solution and mixed well. Then, different masses of LM (0.08, 0.11, 0.14, 0.18, 0.17 and 0.20 g) were added. The composite solution was sonicated for 30 min.

2.5 Preparation of hybrid inks for TPU with Ag, Ag NWs and carbon (TPU@Ag ink-2, TPU@Ag NWs ink-2 and TPU@Carbon ink-2)

Ag powder, Ag NWs solution and carbon black powder were added to 4 mL TPU electrospinning solution and sonicated for 35 min.

2.6 Fabrication of LM electrospinning electrodes (LMEE)

Applied voltages: − 2–13 V, solution flow rate: 1.0 mL·h^{-1}, distance: 18 cm. The TPU substrate was obtained after electrospinning for 70 min. Next, PaLMP ink-1 was brushed on the substrate. Finally, it was laser marked (Galvo Scanner RC1001, power of 0.15·W) to activate the ink.

2.7 Fabrication of dielectric layers

TPU@LM fiber-based dielectric layer was obtained by TPU@LM ink-2 via electrospinning (35 min). TPU@Ag, TPU@Ag NWs and TPU@Carbon fiber-based dielectric layers were prepared as above.

2.8 Fabrication of all-fiber anti-jamming stretchable capacitive pressure sensor

Electrospinning of TPU@LM ink-2 on LMEE for 35 min was prepared to deposit a thin film of TPU @LM fibers, which acted as a dielectric layer. Other dielectric layers were prepared by similar methods. The TPU@LM sensor was then completed.

2.9 Characterization

The morphology and composition were characterized using the scanning electron microscope (SEM, FEI Nova Nano-SEM 450, SU1510 Hitachi and ZEISS Sigma 300). A four-point probe (Xinyang CXT-2663) was used to characterize the square resistance. The dielectric constant was characterized via a broadband dielectric impedance spectrometer (HC-E4990A). Mechanical and stability testing was accomplished using a tensile machine (Yuelian YL-S71) and a linear motor instrument (LinMot E1100). Zata potential and particle size characterization were carried out using the dynamic light scattering (DLS, Malvern Zetasizer Nano ZS ZEN3600). All resistance and capacitance signals of electrodes and sensors were tested using an inductance–capacitance–resistance (LCR) meter (E980-AL-30).

The sensitivity and detection ranges were measured by an LCR measuring instrument (E980-AL-30) and its software, a tensile machine. The positive and negative copper wires of the sensor were connected to the two clamps of the LCR meter, and the LCR meter was operated at a frequency of 80 kHz. Different pressures were applied to the device using the stretching machine, the pressure application rate was 3 mm·min^{-1}, and the data acquisition was performed using the LCR measuring instrument. Cyclic stability test under pressure is measured using a linear motor, dynamometer and LCR meter. A fixed impact pressure was used. The linear motor repeatedly impacts the device. After repeated loading and unloading of the pressure, the LCR meter records the change in the capacitance value of the sensor each time it is pressurized.

3 Results and discussion

3.1 Design concept of all-fiber anti-jamming capacitive pressure sensors

Stretchability, breathability, biocompatibility and heat dissipation are critical for the long-term use of wearable devices. The development of electrospinning technology has laid the foundation for the development of all-fiber wearable devices. However, conventional electrospinning polymer materials tend to exhibit low dielectric constants, making the dielectric layer highly susceptible to environmental interference, thereby undermining the accuracy and stability of the output signal. To address this challenge, LMs were introduced as functional materials into nanofibers. As shown in Fig. 1a, the modified LM particles were mixed with TPU solution for electrospinning to obtain a dielectric layer, which was then assembled with an LMEE to fabricate an all-fiber anti-jamming capacitive pressure sensor. The pressure response can resist interference signals generated in various noisy environments, resulting in a high SNR. It can be connected to human joints as a wearable device for physiological signal monitoring. The left of Fig. 1b shows a schematic image where the LM particles are encapsulated in the nanofibers. On the right is a SEM image of the nanofibers, with the blended nanofibers as a spider web.

3.2 Preparation and characterization of mechanical properties

The all-fiber anti-jamming capacitive pressure sensor based on modified LM consists of two functional layers: LMEE and TPU@LM dielectric layer. The preparation process is shown in Fig. 2a. The LMEE was made conductive by brushing LM-modified ink (PaLMP ink-1) [76] onto the TPU electrospinning substrate and then activating the ink using a laser marker. Subsequently, TPU@LM ink-2 was electrostatically spun on LMEE to serve as the dielectric

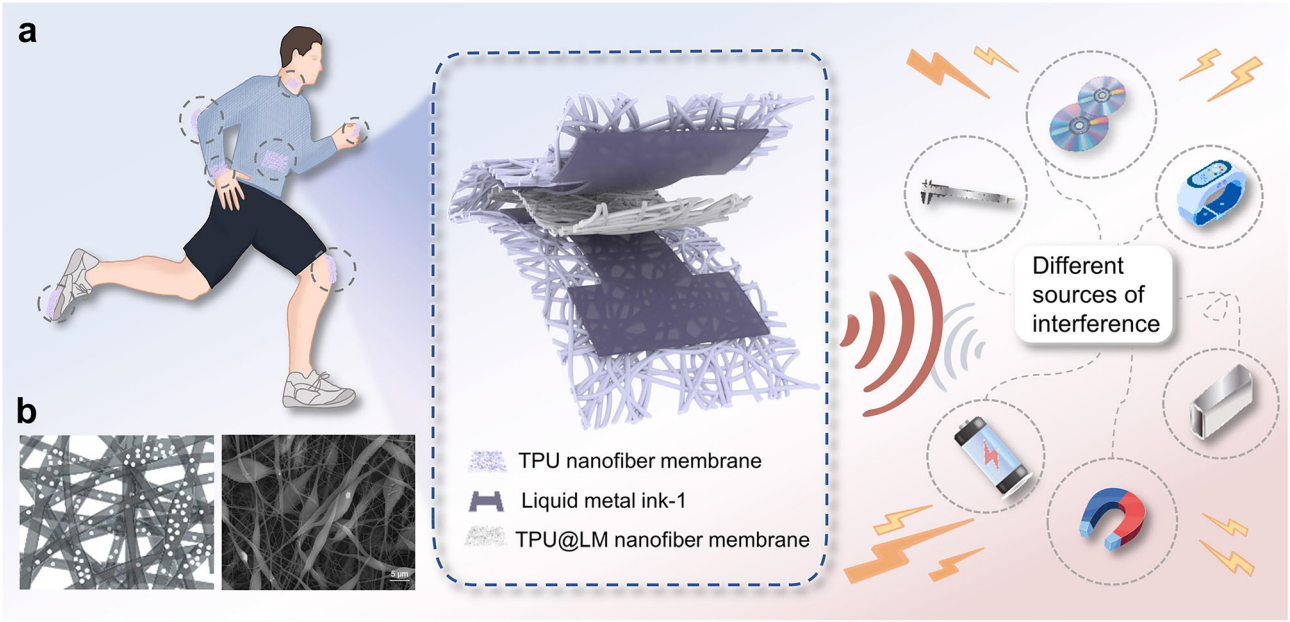

Fig. 1 **a** All-fiber anti-jamming capacitive pressure sensor applied to real-time monitoring of multiple physiological signals; **b** schematic microstructure of TPU@LM fiber dielectric layer (left) and SEM image (right)

layer for the sensor. Finally, the LMEE was assembled with a dielectric layer to obtain the TPU@LM capacitive sensor. Then, the influence of fiber-based dielectric layers obtained from different substances and TPU was explored. As shown in Fig. S1, TPU@LM ink-2 was obtained by tip ultrasonication. As a surfactant, PSS stabilized the dispersion of LM, resolving issues of high surface tension and poor wettability. TPU@LM, TPU@Ag, TPU@Carbon and TPU@Ag NWs fiber-type dielectric layers were obtained by hybrid electrospinning. Figure S2 demonstrates the excellent stretchability of the TPU@LM fiber dielectric layer. Stress–strain tests were conducted after ensuring nearly identical dielectric constants among the samples (the difference between the maximum value and the minimum value was 0.037) (Fig. 2b). The mechanical properties of the TPU@LM, TPU@Ag, TPU@Ag NWs and TPU@Carbon fiber-based dielectric layers were compared with pure TPU fiber-based dielectric layers in Fig. 2c. The ultimate fracture stress and strain of the TPU@LM fiber-based dielectric layers are 928.386 kPa and 167.5%, respectively. The fluidity and flexibility of LM, combined with the good flexibility and tensile properties of TPU fibers, result in increased softness. When the two flexible phases exist, the fracture strain of the TPU@LM fiber-based dielectric layer gradually increases, and the stress gradually decreases. Conversely, the incorporation of Ag powder, carbon black powder, and Ag NWs as a rigid phase increased the toughness of the fiber. Figure 2c also demonstrates that they all have higher stress while they have less strain than the TPU@LM fiber-based dielectric layer. As shown in Fig. 2d, Young's modulus of TPU@LM, pure TPU, TPU@Ag NWs, TPU@Carbon and TPU@Ag fiber-based dielectric layers are (2.145 ± 0.005), (5.348262 ± 0.070), (8.880 ± 0.031), (9.249 ± 0.033) and (11.400 ± 0.044) kPa, respectively, further indicating that the presence of LM decreases Young's modulus of TPU fibers. Figure 2e shows the energy-dispersive X-ray spectroscopy (EDS) maps of the TPU@LM dielectric layer, which shows that LM exists in the fiber through the distribution of Ga and In elements (C and O are the main elements of the fiber), with SEM image (Fig. 1c) confirming the effective integration of LM with TPU fibers. Figure S3 demonstrates the flexibility of the device. Figure 2f, g explores its sensing performance under different strain conditions. At the initial instant of strain, the capacitance value of the device shows a small peak. This is due to a short, sharp rise in capacitance value when the device is suddenly subjected to a large strain (Fig. 2f). However, the capacitance value can gradually stabilize when the continuous strain remains over 60 s (Fig. S4). In addition, Fig. 2g specifically demonstrates the sensor's sensitivity over the 0–120% strain range, showing good linearity and stable capacitive response. Further validating its excellent strain sensing performance, the inset visualizes an optical photograph of the sensor before and after stretching. Figure S5 shows that the capacitive output signal of the device remains stable during more than 10,000 cycles at a strain of 50%. It is further explained that the sensor has excellent durability.

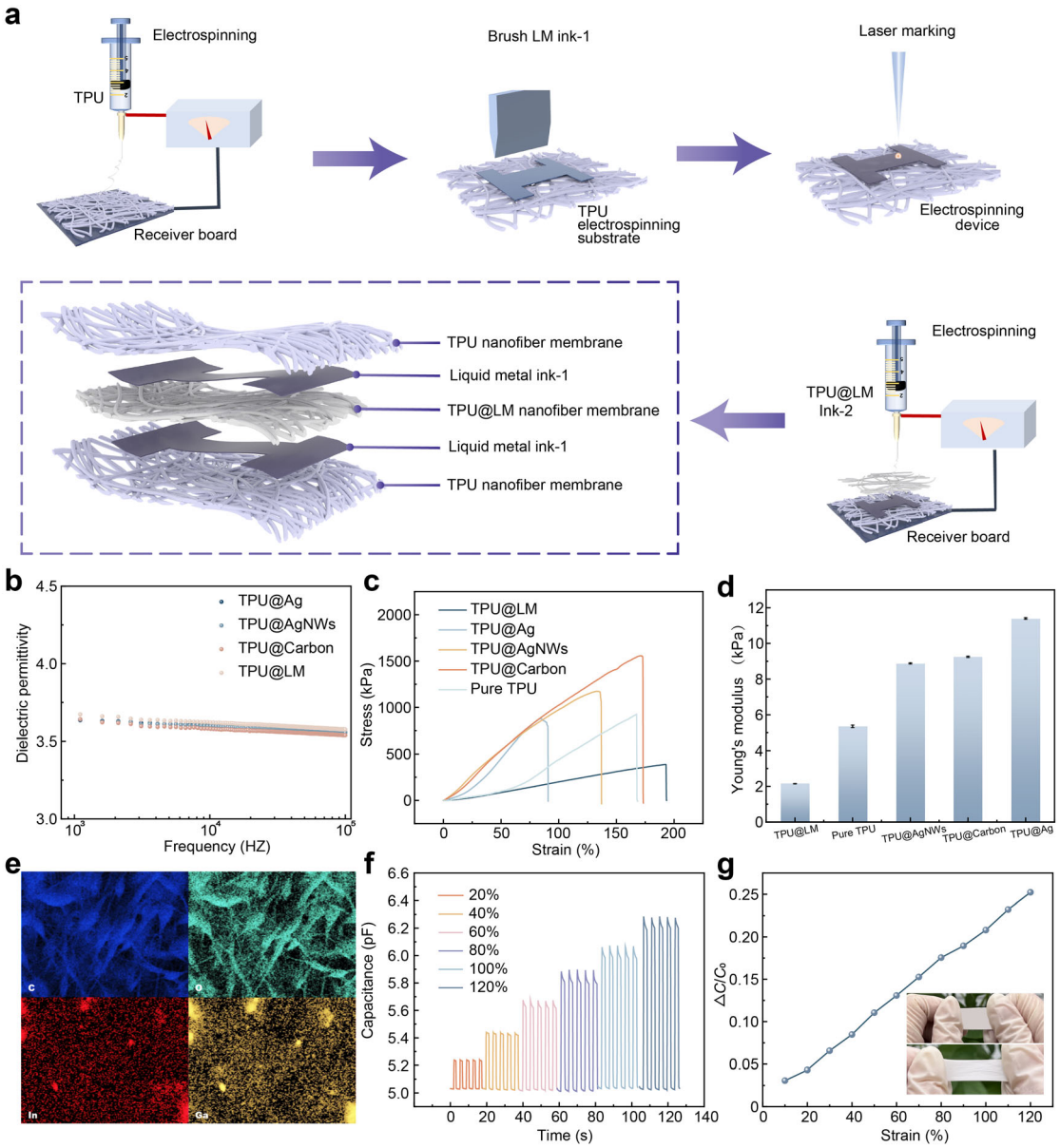

Fig. 2 Preparation process and strain sensing performance characterization test: **a** schematic representation of preparation procedure of TPU@LM sensor; **b** relationship between dielectric constant and frequency of electrospinning fiber membranes of TPU@LM, TPU@Ag, TPU@Carbon and TPU@Ag NWs; **c** uniaxial tensile stress–strain curves of four fiber-based dielectric layers (TPU@LM, TPU@Ag, TPU@Carbon and TPU@Ag NWs); **d** comparison of Young's modulus of four electrospinning fiber membranes; **e** EDS maps of electrospinning fiber membrane of TPU@LM; **f** variation of capacitance value of TPU@LM sensor under different strains; **g** sensing performance test of TPU@LM sensor at 0%–120% strain and (inset) optical images of sensor before and after stretching

The mechanical and sensing properties of the dielectric layer significantly impact sensor performance, and electrodes that operate stably with resistance insensitive to strain are also crucial for enhancing sensor performance. Among them, PaLMP ink-1 was prepared, as shown in Fig. S6, involving a solution composed of LM and PSS in deionized water (DI) with AA. The zeta potential (ζ) and EDS maps confirmed that PSS encapsulated LM particles through electrostatic interaction (carbon is the main element of PSS, Fig. S7a, b). The modified LM particles can be well dispersed and stably stored in solution, and these LM particles surrounded by PSS are referred to as PaLMP, and LMP means LM particles without PSS. Figure S8 demonstrates the particle size of both PaLMP and LMP particles. The close packing of PaLMP particles requires the indispensable role of AA. The wettability of LM, LMP

and PaLMP was compared by the contact angle (Fig. S9a). The characterization of PaLMP showed that this strategy could enhance wettability and reduce the surface tension of LM. Figure S9b further demonstrates the contact angle values of PaLMP on other substrates with values $\leq 90°$. The remarkable effectiveness of the modification strategy in improving its wettability with different substrates is reconfirmed. Then, the mechanical properties of LMEE were characterized. The morphology of this electrode before and after laser activation is shown in Fig. S10a, b. After activation of PaLMP, the internal LM outflow wraps around the fibers, forming a conductive fiber and pathway, which can also be indicated from the bar-like fibers as the distribution of the Ga and In elements in the EDS maps (Fig. S10c). Figure S11a shows the squared resistance of five LMEEs with varying PSS contents. The strain conductivity performance of these LMEEs was also evaluated, with LMEE (0.25 wt%) demonstrating a resistance change of 16% at a strain of 230% (Fig. S11b), indicating lower square resistance and better strain conductivity performance. Therefore, LMEE (0.25 wt%) was selected for subsequent electrodes. Finally, LMEE (0.25 wt%) was subjected to a cyclic stability test, and it exhibited stable responses without electrical failures under repeated strain and retraction over 14,000 cycles (Fig. S11c).

3.3 Characterization of sensing and anti-jamming performance of devices

Capacitive pressure sensors with long-term stable sensing performance hold significant importance for practical applications. The addition of metal or conductive particles to polymer films can improve their dielectric properties. As a result, the dielectric properties and Young's modulus are also altered by the addition of LM. This ultimately affects the compressive deformation capability of the sensor, which provides a key strategy for the improvement of sensing performance. Therefore, there exists an optimum value for LM doping. When LM doping is excessive, it affects Young's modulus of the materials and the detection range of the device. Figure 3a presents the parameter optimization test of the sensor. This is accomplished by altering the LM content within the dielectric layer. The pressure sensing performance of TPU@LM capacitive sensors with different parameters is compared with the sensor integrated with a pure TPU fiber-based dielectric layer (the pure TPU capacitive sensor). The higher sensor sensitivity can be achieved when the LM doping content is 5.5 wt%. Typically, $S = (\Delta C/C_0)/\Delta P$ is commonly used to calculate the sensitivity (S), where ΔC represents the relative capacitance change and ΔP represents the applied pressure change. However, C_0 will change to a certain extent in different environments, resulting in the relative change in the value of capacitance being sensitive. Here, we utilize $\Delta C/\Delta P$ to calculate the average pressure sensitivity (S'). Characterization based on the absolute change in capacitance provides a more realistic response to the pressure detection performance [77]. Thus, the device (5.5·wt%) has a sensitivity of 0.324 $pF{\cdot}kPa^{-1}$ in the detection range of 0–50 kPa, while in the 50–300 kPa detection range, it is 0.066 $pF{\cdot}kPa^{-1}$ with a 0.99 fitted linearity. In the detection range of 300–2100 kPa, the sensitivity of 0.023 $pF{\cdot}kPa^{-1}$ with a 0.99 fitted linearity is obtained. It can be seen that the sensor has a wide detection range. We then tested the device (5.5 wt%) at different pressures (Fig. 3b). The stable response under different pressures proves high sensitivity likewise. Figure 3c shows its dynamic loading–unloading response time of 161.5 and 178.3 ms, respectively. Further, the steady-state step response was tested at different pressures. The device exhibited a relatively stable capacitance signal as the pressure was gradually increased and decreased. When the external pressure is reduced to zero, the capacitance value returns to its initial state in time. Its stable performance under continuous loading was confirmed (Fig. 3d). However, the device was assembled with very high bond (VHB) around the periphery, and the viscoelasticity of the VHB resulted in a less pronounced step response from 0 to 25 kPa. Subsequently, the cyclic stability performance was tested. Figure 3e shows that the sensor can still respond stably under high pressure of 105 kPa and up to 20,000 loading–unloading cycles. It shows the potential for long-term and stable pressure detection. The practical effects of ambient temperature changes on the performance of the TPU@LM sensor were further explored. With the gradual increase in ambient temperature, the absolute change in capacitance value of the TPU@LM sensor was insignificant (Fig. S12). Therefore, the effect of ambient temperature on the sensing performance is negligible in practical applications. The sensor demonstrated excellent stability over a wide temperature range. Finally, we compared the overall performance between TPU@LM sensors and previously reported flexible capacitive pressure sensors (Table S1). The device demonstrated outstanding sensing performance and a wide detection range.

To demonstrate the anti-interference performance of the devices, they were placed in different environments. The enhanced anti-jamming performance is verified by generating interference at close range and electromagnetic waves. The capacitance signal was interfered with common materials: CD, iron, battery, skin and the electromagnetic wave from an electronic watch (Fig. 4a). When faced with the proximity of an interference source, the amplitude of capacitance change is tiny. In the presence of a normal pressure signal response, this change can be disregarded. When the interference source ceases to operate, the change

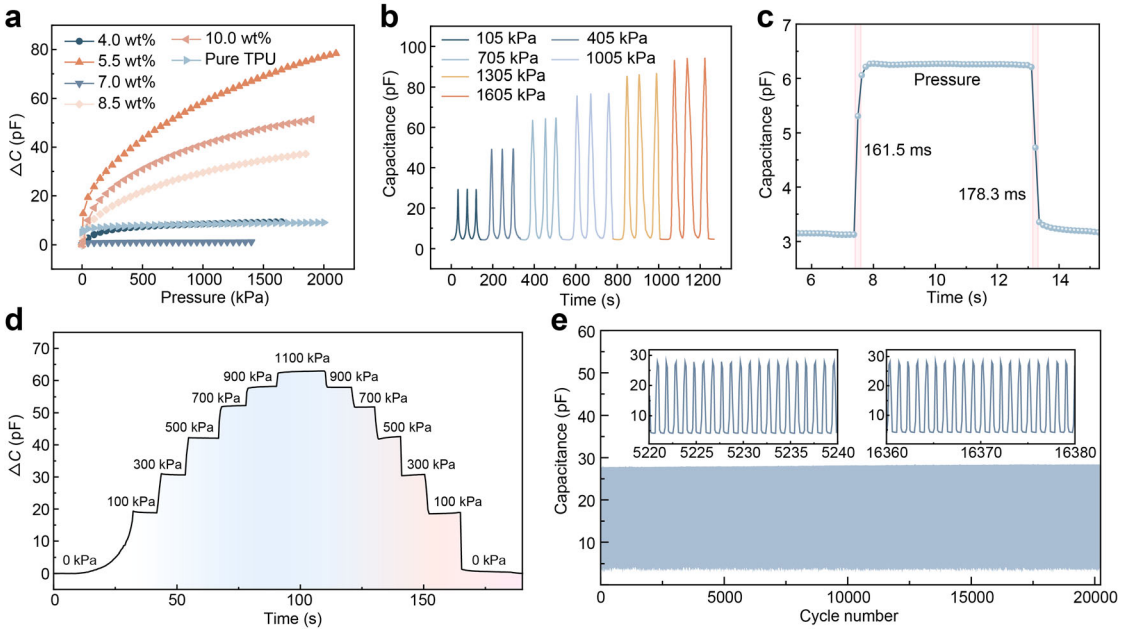

Fig. 3 Sensing performance of TPU@LM capacitive sensor: **a** influence of different LM doping contents on sensor performance; **b** dynamic response to various external pressures; **c** response and recovery time; **d** steady-state step response test to different pressures; **e** stable performance test under 105 kPa with over 20,000 loading–unloading pressure cycles

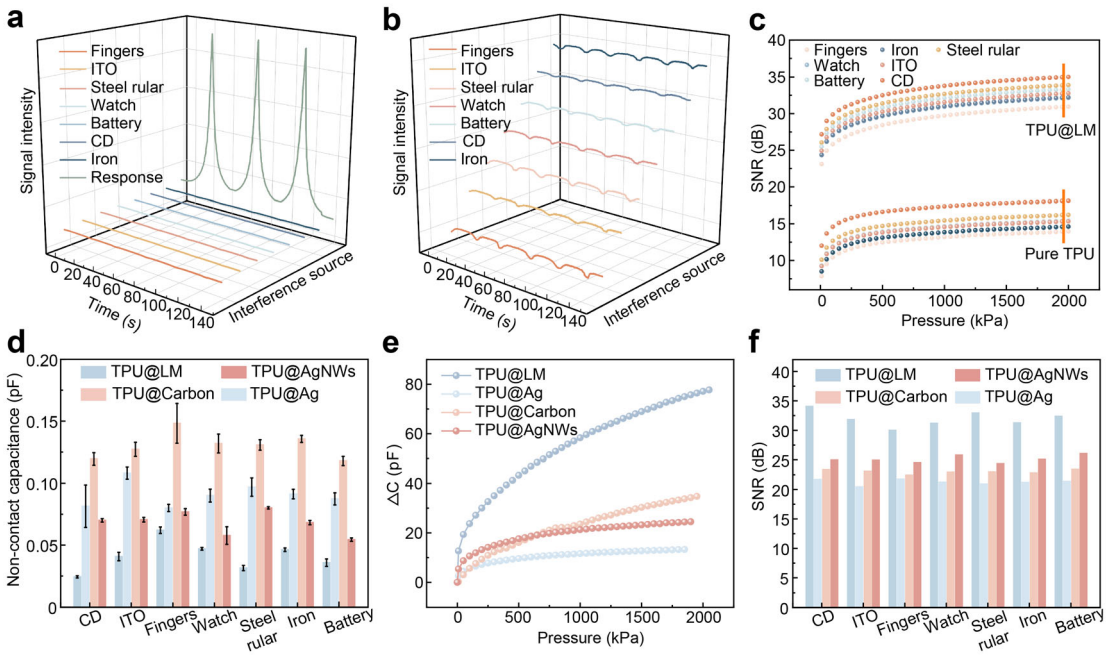

Fig. 4 Anti-jamming performance tests: **a** comparison of pressure response signal and intensity of seven interference signals; **b** demonstration of fluctuations of seven interference signals; **c** comparison of SNR of TPU@LM sensor and pure TPU sensor; **d** relative capacitance changes of four sensors (TPU@LM, TPU@Ag, TPU@Carbon and TPU@Ag NWs) in non-contact interference under various interference; **e** capacitance value change of four sensors under pressure; **f** comparison of SNR of four sensors under seven interference sources

in capacitance value can be obtained in Fig. 4b. We also compared the anti-jamming capabilities of TPU@LM capacitive sensors and pure TPU capacitive sensors (Fig. 4c). In different interference sources, the SNR of TPU@LM sensors is nearly three times greater than that of pure TPU capacitive sensors. In calculating the SNR, it can be based on the following equation:

$$\mathrm{SNR} = 10\ \lg(P_s/P_n) \quad (1)$$

where SNR is measured in decibels (dB), P_s is the average power of the effective pressure signal, and P_n is the average power of the noise signal. To further prove that the doping of LM has a higher SNR compared to other dopants. Figure 4d shows the variation of non-contact capacitance values of TPU@LM, TPU@Ag, TPU@Carbon and TPU@Ag NWs capacitive sensors in different interference sources. The capacitance changes of TPU@LM capacitive sensors are less than 0.1 pF, which is smaller than other sensors. However, we found that the TPU@LM capacitive sensor is much higher than the other sensors in the effective pressure response, and it also has a wider detection range (Fig. 4e). It is found that the doping of LM increases the dielectric properties, which leads to an increase in the detection sensitivity. Finally, the SNR of the TPU@LM capacitive sensor is higher than 27.5 dB at a pressure of 1150 kPa and under seven interference conditions, which is also higher than other sensors (Fig. 4f). The greater anti-jamming performance is well demonstrated (data at multiple pressures are shown in Fig. S13). The superior anti-jamming performance lays a solid foundation for circuit integration.

3.4 Application of device for monitoring physiological signals

Wearable electronic devices are primarily used to monitor and record the physiological signals of the human body, which can provide support for personal health, sports exercise, medical diagnosis and so on. To evaluate the practical application performance, it is attached to multiple locations on the human body for signal acquisition. As shown in Fig. 5a, the sensor was attached to the vocal cords in the neck. When sound is emitted, the vocal cords vibrate, and the sensor can respond quickly and stably. As the sound increases, the amplitude of the vocal fold vibration increases, and the value of the capacitive signal change also increases. Conversely, the capacitive signal change decreases as the sound decreases. Figure 5b shows the capacitance signal change when the elbow is bent, and the capacitance change is basically stable and consistent at the same bending amplitude. We also attached it to the wrist, and there is a clear difference at four different bending angles. The larger the bending angle, the larger the pressure the sensor feels, and the larger the change in capacitance value (Fig. 5c). Figure 5d shows the signal amplitude change under six bending angles of the finger. When the bending angle gradually increases and decreases, the capacitance value change shows a stepwise increase and decreases. When the finger returns to the horizontal straight state, the capacitance returns to the initial value. This also demonstrates the sensor's ability to monitor the subtle movements of human joints. It is worth noting that the thickness of the VHB tape itself affects the device's performance. At the stage when the finger first starts to bend, the point of force is not immediately concentrated in the middle of the device. As a result, the sensor is affected by the viscoelasticity of the VHB tape during the initial bending of the finger to 45°, resulting in a less pronounced step response at the start of the device. In addition, when the finger is restored to a horizontal angle, the capacitive response of the device is slightly slower in recovery due to the strong adhesion of the medical PU tape, and the step response is not prominent enough. However, after a certain period of time, the capacitive response stabilizes. Figure 5e, g demonstrates the ability to maintain a stable and fast response to real-time motion monitoring of the knee and the sole of the foot, respectively. Figure 5f shows the device attached to the belly to detect subtle changes in breathing. The sensor can clearly capture physiological signals such as sound, breathing and movement, helping to better understand the physical condition, detect potential health problems in time and take appropriate measures for prevention and intervention. Subsequently, the anti-jamming performance in practical applications was also evaluated. A pure TPU capacitive sensor was used as a non-interference-resistant (N-I-R) device, compared with a TPU@LM capacitive sensor as an anti-jamming device. The volunteer wore the device on the sole of the forefoot and stood on a wooden table (with a height of 70 cm) as well as on the floor to acquire capacitive signals. The ground is a large conductor and can interfere with the capacitance sensor, causing a large change in its capacitance value. However, the wooden table has no applied capacitance to affect it due to its distance from the ground. Figure 5h depicts the magnitude of the signal change when the experimenter is standing on the ground with the N-I-R sensor vs. on the table. It can be observed that the N-I-R sensor is more affected when it is on the ground, suggesting that the device is incapable of achieving interference-resistant performance. In Fig. 5i, with the anti-jamming device, the amplitude of capacitance change is essentially the same whether the volunteer is standing on a table or the ground, which proves that the anti-jamming device is more accurate, reliable, and stable in practical applications.

4 Conclusion

In summary, we innovatively proposed a method to prepare a fiber dielectric layer based on hybrid electrospinning of modified LM and TPU, which improves the dielectric properties of the nanofiber dielectric layer while ensuring the stretchability and improves the anti-jamming of

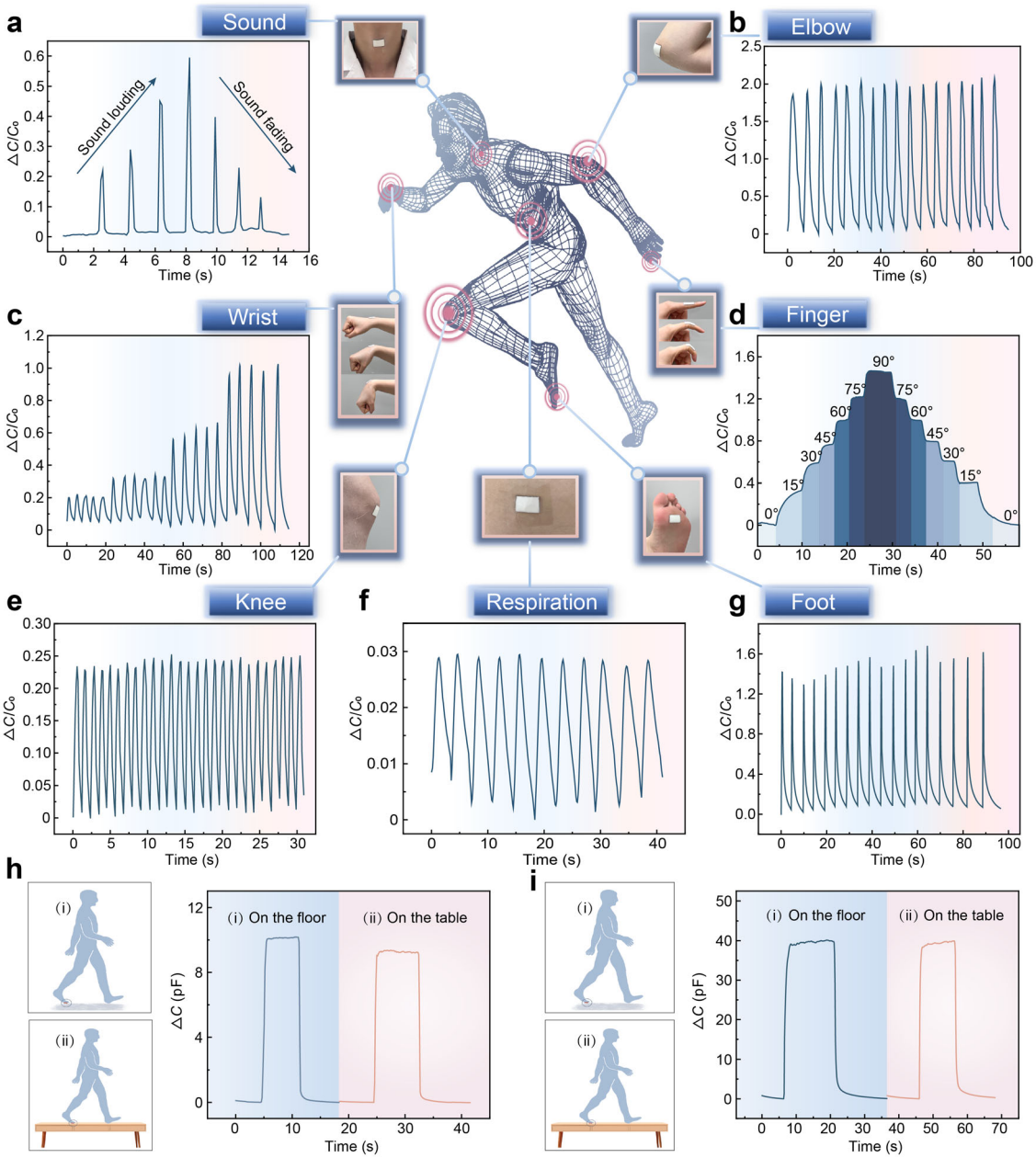

Fig. 5 Application of TPU@LM sensor in physiological signal monitoring: **a** attached to position of vocal cords in neck to monitor changes in sound volume; **b** fixed at elbow to monitor elbow flexion changes; **c** on wrist to detect different degrees of bending movements; **d** on knuckle to detect finger bending angle; **e**, **g** attached to knees and soles to monitor physiological signals during exercise; **f** attached to stomach to monitor breathing changes; magnitude of capacitance changes on ground and a wooden table for **h** a pure TPU and **i** a TPU@LM capacitive sensor worn on forefoot

capacitive pressure sensors. The modified LM was embedded into the nanofibers, which improved the dielectric properties of the fiber-based dielectric layer. In tests with various interference sources close to the device, the SNR is higher than 27.5 dB, nearly three times that of a pure TPU capacitive sensor. Noise signal fluctuations are negligible. It demonstrates stronger immunity to interference than conventional capacitive pressure sensors. In addition, by replacing the traditional functional filler with LM, the fabricated TPU@LM composites have a low

Young's modulus and high elongation at break, resulting in a sensor with a broad detection range. The excellent stretchability provides that the all-fiber-based devices have better flexibility and adaptability, which can be better adapted to the needs of different application scenarios. Finally, it is demonstrated as a wearable device that captures various physiological parameters such as respiration and movement status of the experimenter in real time, while resisting external interference signals in practical applications. This work provides a new idea for the development of stretchable and anti-jamming capacitive pressure sensors, which is expected to potentially drive further innovation and development in wearable devices and medical health monitoring.

Acknowledgements This study was financially supported by the National Natural Science Foundation of China (Nos. U20A20166, 52371202, 52125205, 52250398, 52192614 and 52003101), the National Key R&D Program of China (No. 2021YFB3200300), the Natural Science Foundation of Beijing Municipality (No. 2222088), Shenzhen Science and Technology Program (No. KQTD20170810105439418) and the Fundamental Research Funds for the Central Universities.

Declarations

Conflict of interests Cao-Feng Pan is an editorial board member for *Rare Metals* and was not involved in the editorial review or the decision to publish this article. All authors declare that there are no competing interests.

References

[1] Wang CF, Dong L, Peng DF, Pan CF. Tactile sensors for advanced intelligent systems. Adv Intell Syst. 2019;1(8):1900090. https://doi.org/10.1002/aisy.201900090.

[2] Tao J, Dong M, Li L, Wang CF, Li J, Liu Y, Bao RR, Pan CF. Real-time pressure mapping smart insole system based on a controllable vertical pore dielectric layer. Microsyst Nanoeng. 2020;6:62. https://doi.org/10.1038/s41378-020-0171-1.

[3] Wei RL, He JQ, Ge SP, Liu H, Ma XL, Tao J, Cui X, Mo XM, Li Z, Wang CF, Pan CF. Self-powered all-optical tactile sensing platform for user-interactive interface. Adv Mater Technol. 2022;8(1):2200757. https://doi.org/10.1002/admt.202200757.

[4] Liu Y, Tao J, Mo YP, Bao RR, Pan CF. Ultrasensitive touch sensor for simultaneous tactile and slip sensing. Adv Mater. 2024;36(21):2313857. https://doi.org/10.1002/adma.202313857.

[5] Liang YG, Lu QC, Wu WQ, Xu ZS, Lu H, He ZJ, Zhu YZ, Yu Y, Han X, Pan CF. A universal fabrication strategy for high-resolution perovskite-based photodetector arrays. Small Methods. 2023;7(9):2300339. https://doi.org/10.1002/smtd.202300339.

[6] Bao RR, Pan CF. Efficient perovskite solar cells with body temperature self-repairing. Sci Bull. 2022;67(22):2263. https://doi.org/10.1016/j.scib.2022.11.003.

[7] Jiang M, Zhang X, Wang F. Enabling monodisperse perovskite phase with buried interface modification toward efficient light-emitting diodes. Nano Res Energy. 2023;2:e9120069. https://doi.org/10.26599/NRE.2023.9120069.

[8] He JQ, Wei RL, Ma XL, Wu WQ, Pan XJ, Sun JL, Tang JQ, Xu ZS, Wang CF, Pan CF. Contactless user-interactive sensing display for human-human and human-machine interactions. Adv Mater. 2024;36(25):2401931. https://doi.org/10.1002/adma.202401931.

[9] Gao NW, Huang JY, Chen ZW, Liang YG, Zhang L, Peng ZC, Pan CF. Biomimetic ion channel regulation for temperature-pressure decoupled tactile perception. Small. 2023;20(1):2302440. https://doi.org/10.1002/smll.202302440.

[10] Lu Y, Wang MY, Wang DY, Sun YH, Liu ZH, Gao RK, Yu LD, Zhang DZ. Flexible impedance sensor based on $Ti_3C_2T_x$ MXene and graphitic carbon nitride nanohybrid for humidity-sensing application with ultrahigh response. Rare Met. 2023;42(7):2204. https://doi.org/10.1007/s12598-023-02268-2.

[11] Yang SY, Yang WK, Yin R, Liu H, Sun HL, Pan CF, Liu CT, Shen CY. Waterproof conductive fiber with microcracked synergistic conductive layer for high-performance tunable wearable strain sensor. Chem Eng J. 2023;453:139716. https://doi.org/10.1016/j.cej.2022.139716.

[12] Gao WC, Huang JY, He J, Zhou RH, Li ZM, Chen ZY, Zhang YF, Pan CF. Recent advances in ultrathin materials and their applications in e-skin. InfoMat. 2023;5(8):e12426. https://doi.org/10.1002/inf2.12426.

[13] He JQ, Wei RL, Ge SP, Wu WQ, Guo JC, Tao J, Wang R, Wang CF, Pan CF. Artificial visual-tactile perception array for enhanced memory and neuromorphic computations. InfoMat. 2023;6(3):e12493. https://doi.org/10.1002/inf2.12493.

[14] Liu Y, Xu HY, Dong M, Han RH, Tao J, Bao RR, Pan CF. Highly sensitive wearable pressure sensor over a wide sensing range enabled by the skin surface-like 3D patterned interwoven structure. Adv Mater Technol. 2022;7(12):2200504. https://doi.org/10.1002/admt.202200504.

[15] He J, Zhou RH, Zhang YF, Gao WC, Chen T, Mai WJ, Pan CF. Strain-insensitive self-powered tactile sensor arrays based on intrinsically stretchable and patternable ultrathin conformal wrinkled graphene-elastomer composite. Adv Funct Mater. 2021;32(10):2107281. https://doi.org/10.1002/adfm.202107281.

[16] Liu Y, Tao J, Yang WK, Zhang YF, Li J, Xie HL, Bao RR, Gao WC, Pan CF. Biodegradable, breathable leaf vein-based tactile sensors with tunable sensitivity and sensing range. Small. 2022;18(8):2106906. https://doi.org/10.1002/smll.202106906.

[17] Zhou KK, Xu WJH, Yu YF, Zhai W, Yuan ZQ, Dai K, Zheng GQ, Mi LW, Pan CF, Liu CT, Shen CY. Tunable and nacre-mimetic multifunctional electronic skins for highly stretchable contact-noncontact sensing. Small. 2021;17(31):2100542. https://doi.org/10.1002/smll.202100542.

[18] He ZP, Han X, Wu WQ, Xu ZS, Pan CF. Recent advances in bioinspired vision systems with curved imaging structures. Rare Met. 2024;43(4):1407. https://doi.org/10.1007/s12598-023-02573-w.

[19] Lv J, Thangavel G, Xin YY, Gao D, Poh WC, Chen SH, Lee PS. Printed sustainable elastomeric conductor for soft electronics. Nat Commun. 2023;14(1):7132. https://doi.org/10.1038/s41467-023-42838-7.

[20] Bao RR, Tao J, Zhao J, Dong M, Li J, Pan CF. Integrated intelligent tactile system for a humanoid robot. Sci Bull. 2023;68(10):1027. https://doi.org/10.1016/j.scib.2023.04.019.

[21] Li YX, Qin HY, Hu C, Sun MM, Li PY, Liu H, Li JC, Li ZB, Wu LD, Zhu J. Research progress of nanomaterials-based sensors for food safety. J Anal Test. 2022;6(4):431. https://doi.org/10.1007/s41664-022-00235-x.

[22] Wan YX, Tao J, Dong M, Zhang L, Peng ZC, Bao RR, Pan CF. Flexible intelligent sensing system for plane complex strain monitoring. Adv Mater Technol. 2022;7(12):2200386. https://doi.org/10.1002/admt.202200386.

[23] Zhang D, Meng X, Hou W, Weihao H, Mo J, Yang T, Zhang W, Fan Q, Liu L, Jiang B, Chu L, Li M. Solid polymer electrolytes: ion conduction mechanisms and enhancement strategies. Nano Res Energy. 2023;2:e9120050. https://doi.org/10.26599/NRE.2023.9120050.
[24] Zheng DG, Lee HD, Lee GW, Shin DS, Kim J, Shim JI, Lin Z, Lee TW, Kim DH. Investigation into charge carrier dynamics in organic light-emitting diodes. Nano Res Energy. 2024;3(2):e9120109. https://doi.org/10.26599/NRE.2024.9120109.
[25] Liu Y, Bao RR, Tao J, Li J, Dong M, Pan CF. Recent progress in tactile sensors and their applications in intelligent systems. Sci Bull. 2020;65(1):70. https://doi.org/10.1016/j.scib.2019.10.021.
[26] Xu HY, Tao J, Liu Y, Mo YP, Bao RR, Pan CF. Fully fibrous large-area tailorable triboelectric nanogenerator based on solution blow spinning technology for energy harvesting and self-powered sensing. Small. 2022;18(37):2202477. https://doi.org/10.1002/smll.202202477.
[27] Huang JY, Zhou RH, Chen ZY, Wang YS, Li ZM, Mo XM, Gao NW, He J, Pan CF. Highly stable and reliable capacitive strain sensor for wearable electronics based on anti-dry hydrogel electrode. Mater Today Phys. 2023;35:101123. https://doi.org/10.1016/j.mtphys.2023.101123.
[28] Lin XZ, Xue H, Li F, Mei HX, Zhao HR, Zhang T. All-nanofibrous ionic capacitive pressure sensor for wearable applications. ACS Appl Mater Interfaces. 2022;14(27):31385. https://doi.org/10.1021/acsami.2c01806.
[29] Qin J, Yin LJ, Hao YN, Zhong SL, Zhang DL, Bi K, Zhang YX, Zhao Y, Dang ZM. Flexible and stretchable capacitive sensors with different microstructures. Adv Mater. 2021;33(34):2008267. https://doi.org/10.1002/adma.202008267.
[30] Sharma S, Chhetry A, Zhang S, Yoon H, Park C, Kim H, Sharifuzzaman M, Hui X, Park JY. Hydrogen-bond-triggered hybrid nanofibrous membrane-based wearable pressure sensor with ultrahigh sensitivity over a broad pressure range. ACS Nano. 2021;15(3):4380. https://doi.org/10.1021/acsnano.0c07847.
[31] Guan FY, Xie Y, Wu HX, Meng Y, Shi Y, Gao M, Zhang ZY, Chen SY, Chen Y, Wang HP, Pei QB. Silver nanowire-bacterial cellulose composite fiber-based sensor for highly sensitive detection of pressure and proximity. ACS Nano. 2020;14(11):15428. https://doi.org/10.1021/acsnano.0c06063.
[32] Yao L, Xinyu Q, Zhao W, Ren Y, Si W, Wang W, Wang Q, Huang W, Dong X. Highly stretchable, elastic, and sensitive MXene-based hydrogel for flexible strain and pressure sensors. Research. 2020;2020:2038560. https://doi.org/10.34133/2020/2038560.
[33] Chen SC, Wang YF, Yang L, Karouta F, Sun K. Electron-induced perpendicular graphene sheets embedded porous carbon film for flexible touch sensors. Nano-Micro Lett. 2020;12(1):136. https://doi.org/10.1007/s40820-020-00480-8.
[34] Yang RX, Dutta A, Li BW, Tiwari N, Zhang WQ, Niu ZY, Gao YY, Erdely D, Xin X, Li TJ, Cheng HY. Iontronic pressure sensor with high sensitivity over ultra-broad linear range enabled by laser-induced gradient micro-pyramids. Liommun. 2023;14(1):2907. https://doi.org/10.1038/s41467-023-38274-2.
[35] Shi ZY, Meng LX, Shi XL, Li HP, Zhang JZ, Sun QQ, Liu XY, Chen JZ, Liu SR. Morphological engineering of sensing materials for flexible pressure sensors and artificial intelligence applications. Nano-Micro Lett. 2022;14(1):141. https://doi.org/10.1007/s40820-022-00874-w.
[36] Yoo D, Won DJ, Cho W, Lim J, Kim J. Double side electromagnetic interference-shielded bending-insensitive capacitive-type flexible touch sensor with linear response over a wide detection range. Adv Mater Technol. 2021;6(11):2100358. https://doi.org/10.1002/admt.202100358.
[37] Ruth SRA, Feig VR, Kim MG, Khan Y, Phong JK, Bao Z. Flexible fringe effect capacitive sensors with simultaneous high-performance contact and non-contact sensing capabilities. Small Struct. 2020;2(2):2000079. https://doi.org/10.1002/sstr.202000079.
[38] Sambyal P, Iqbal A, Hong J, Kim MK, Kim ID, Koo CM. Conductive MXene composites with liquid metal for high-performance electromagnetic interference shielding. Mater Chem Phys. 2023;295:127184. https://doi.org/10.1016/j.matchemphys.2022.127184.
[39] Wang H, Kow J, Raske N, Boer G, Ghajari M, Hewson R, Alazmani A, Culmer P. Robust and high-performance soft inductive tactile sensors based on the Eddy-current effect. Sens Actuator A-Phys. 2018;271:44. https://doi.org/10.1016/j.sna.2017.12.060.
[40] Yuan JK, Yao SH, Dang ZM, Sylvestre A, Genestoux M, Bai J. Giant dielectric permittivity nanocomposites: realizing true potential of pristine carbon nanotubes in polyvinylidene fluoride matrix through an enhanced interfacial interaction. Phys Chem C. 2011;115(13):5515. https://doi.org/10.1021/jp1117163.
[41] Chhetry A, Sharma S, Yoon H, Ko S, Park JY. Enhanced sensitivity of capacitive pressure and strain sensor based on $CaCu_3Ti_4O_{12}$ wrapped hybrid sponge for wearable applications. Adv Funct Mater. 2020;30(31):1910020. https://doi.org/10.1002/adfm.201910020.
[42] Yin RY, Li YH, Li WD, Gao F, Chen X, Li TY, Liang JG, Zhang HL, Gao HF, Li PW, Zhou YL. High-temperature flexible electric Piezo/pyroelectric bifunctional sensor with excellent output performance based on thermal-cyclized electrospun PAN/$Zn(Ac)_2$ nanofiber mat. Nano Energy. 2024;124:109488. https://doi.org/10.1016/j.nanoen.2024.109488.
[43] Zhou YL, Cheng WN, Bai YZ, Hou C, Li K, Huang YA. Rise of flexible high-temperature electronics. Rare Met. 2023;42(6):1773. https://doi.org/10.1007/s12598-023-02298-w.
[44] Jiaqi T, Wang M, Li W, Jiangtao S, Li Y, Lv Z, Li H, Feng X, Chen X. Electronic skins with multimodal sensing and perception. Soft Sci. 2023;3(3):25. https://doi.org/10.20517/ss.2023.15.
[45] Wang S, Nie Y, Zhu H, Yurui X, Cao S, Zhang J, Li Y, Wang J, Ning X, Kong D. Intrinsically stretchable electronics with ultrahigh deformability to monitor dynamically moving organs. Sci Adv. 2022;8(13):15511. https://doi.org/10.1126/sciadv.abl5511.
[46] Xia YF, Zhu Y, Zhi XR, Guo WY, Yang B, Zhang SY, Li MY, Wang X, Pan CF. Transparent self-healing anti-freezing ionogel for monolayered triboelectric nanogenerator and electromagnetic energy-based touch panel. Adv Mater. 2024;36(8):2308424. https://doi.org/10.1002/adma.202308424.
[47] Qu YP, Hao M, Luan XN, Yang QY, Ding JF, Zhou L, Liang GM, Wang FZ, Xie PT, Wu HK. Regulation mechanism of epsilon-negative monolayer graphene/$CaCu_3Ti_4O_{12}$ metacomposites for boosting electromagnetic shielding. Adv Compos Hybrid Mater. 2024;7(2):38. https://doi.org/10.1007/s42114-024-00852-3.
[48] Qu YP, Zhou YL, Yang QY, Cao J, Liu Y, Qi XS, Jiang S. Lignin-derived lightweight carbon aerogels for tunable epsilon-negative response. Adv Sci. 2024;11(26):2401767. https://doi.org/10.1002/advs.202401767.
[49] Qu YP, Du Y, Fan GH, Xin JH, Liu Y, Xie PT, You SX, Zhang ZD, Sun K, Fan RH. Low-temperature sintering Graphene/$CaCu_3Ti_4O_{12}$ nanocomposites with tunable negative permittivity. J Alloy Compd. 2019;771:699. https://doi.org/10.1016/j.jallcom.2018.09.049.
[50] Qu YP, Wu HK, Xie PT, Zeng N, Chen YL, Gong X, Yang JL, Peng Q, Xie Y, Qi XS. Carbon nanotube-carbon black/$CaCu_3Ti_4O_{12}$ ternary metacomposites with tunable negative permittivity and thermal conductivity fabricated by spark plasma

sintering. Rare Met. 2023;42(12):4201. https://doi.org/10.1007/s12598-023-02346-5.
[51] Zhou YL, Wang SL, Yin JY, Wang JJ, Manshaii F, Xiao X, Zhang TQ, Bao H, Jiang S, Chen J. Flexible metasurfaces for multifunctional interfaces. ACS Nano. 2024;18(4):2685. https://doi.org/10.1021/acsnano.3c09310.
[52] Yue Y, Li X, Zhao Z, Wang H, Guo X. Stretchable flexible sensors for smart tires based on laser-induced graphene technology. Soft Sci. 2023;3(2):13. https://doi.org/10.20517/ss.2023.02.
[53] Han RH, Liu Y, Mo YP, Xu HC, Yang ZW, Bao RR, Pan CF. High anti-jamming flexible capacitive pressure sensors based on core–shell structured AgNWs@TiO_2. Adv Funct Mater. 2023;33(51):2305531. https://doi.org/10.1002/adfm.202305531.
[54] Wang HR, Jiang Y, Ma ZW, Shi YQ, Zhu YJ, Huang RZ, Feng YZ, Wang ZB, Hong M, Gao JF, Tang LC, Song PA. Hyperelastic, robust, fire-safe multifunctional MXene aerogels with unprecedented electromagnetic interference shielding efficiency. Adv Funct Mater. 2023;33(49):2306884. https://doi.org/10.1002/adfm.202306884.
[55] Xu LJ, Wang LD, Zhang WQ, Xue J, Hou SF. The reinforced electromagnetic interference shielding performance of thermal reduced graphene oxide films via polyimide pyrolysis. ACS Omega. 2022;7(13):10955. https://doi.org/10.1021/acsomega.1c06767.
[56] Zhang WJ, Huang L, Mi XJ, Xie HF, Feng X, Ahn JH. Researches for higher electrical conductivity copper-based materials. cMat. 2024;1(13):23. https://doi.org/10.1002/cmt2.13.
[57] Zhou RH, Huang JY, Li ZM, Wang YS, Chen ZY, Pan CF. High precision patternable liquid metal based conductor and adhesive substrate enabled stretchable hybrid systems. Nano Res. 2024;17:5595. https://doi.org/10.1007/s12274-024-6516-6.
[58] Liu AP, Chen ZX, Wang ZH, Fang L, Huang YZ. Two-dimensional Mxenes-Ag micro-nano mixed film for surface-enhanced Raman research. Chin J Rare Met. 2022;46(8):989. https://doi.org/10.13373/j.cnki.cjrm.XY22060028.
[59] Lin RZ, Kim HJ, Achavananthadith S, Xiong Z, Jason KWL, Kong YL, Ho JS. Digitally-embroidered liquid metal electronic textiles for wearable wireless systems. Nat Commun. 2022;13(1):2190. https://doi.org/10.1038/s41467-022-29859-4.
[60] Tao PD, Wang SG, Chen L, Ying JF, Lv L, Sun LW, Chu WB, Nishimura K, Fu L, Wang YZ, Yu JH, Jiang N, Dai W, Lv YK, Lin CT, Yan QW. Enhancement of in-plane thermal conductivity of flexible boron nitride heat spreaders by micro/nanovoid filling using deformable liquid metal nanoparticles. Rare Met. 2023;42(11):3662. https://doi.org/10.1007/s12598-023-02400-2.
[61] Pan XJ, Xu ZS, Bao RR, Pan CF. Research progress in stretchable circuits: Materials, methods and applications. Adv Sensor Res. 2023;2(11):2300065. https://doi.org/10.1002/adsr.202300065.
[62] Zhang XD, Zhang ZT, Wang HZ, Cao BY. Thermal interface materials with high thermal conductivity and low Young's modulus using a solid-liquid metal codoping strategy. ACS Appl Mater Interfaces. 2023;15(2):3534. https://doi.org/10.1021/acsami.2c20713.
[63] Tian Y, Qi HC, Wu HP, Zhang DX. Friction behavior of gecko-inspired polydimethylsiloxane micropillar array with tailored Young's modulus by incorporation of ZrO_2 particles. Chem Phys Lett. 2021;763:138202. https://doi.org/10.1016/j.cplett.2020.138202.
[64] Yang J, Tang D, Ao J, Ghosh T, Neumann TV, Zhang D, Piskarev Y, Yu T, Truong VK, Xie K, Lai YC, Li Y, Dickey MD. Ultrasoft liquid metal elastomer foams with positive and negative piezopermittivity for tactile sensing. Adv Funct Mater. 2020;30(36):2002611. https://doi.org/10.1002/adfm.202002611.
[65] Zhuang QN, Ma ZJ, Gao Y, Zhang YK, Wang SC, Lu X, Hu H, Cheung CF, Huang QY, Zheng ZJ. Liquid-metal-superlyophilic and conductivity-strain-enhancing scaffold for permeable superelastic conductors. Adv Funct Mater. 2021;31(47):2105587. https://doi.org/10.1002/adfm.202105587.
[66] Lin MF, Xiong J, Wang J, Parida K, Lee PS. Core-shell nanofiber mats for tactile pressure sensor and nanogenerator applications. Nano Energy. 2018;44:248. https://doi.org/10.1016/j.nanoen.2017.12.004.
[67] Zhang M, Li B, Wang JJ, Huang HB, Zhang L, Chen LQ. Polymer dielectrics with simultaneous ultrahigh energy density and low loss. Adv Mater. 2021;33(22):2008198. https://doi.org/10.1002/adma.202008198.
[68] Shi YQ, Zhang ZY, Huang QY, Lin YJ, Zheng ZJ. Wearable sweat biosensors on textiles for health monitoring. J Semicond. 2023;44(2):021601. https://doi.org/10.1088/1674-4926/44/2/021601.
[69] Hua QL, Shen GZ. A wearable sweat patch for non-invasive and wireless monitoring inflammatory status. J Semicond. 2023;44(10):100401. https://doi.org/10.1088/1674-4926/44/10/100401.
[70] Kwok HS, Fan ZY. Preface to special issue on advanced optoelectronic and electronic devices toward future displays. J Semicond. 2023;44(9):090101. https://doi.org/10.1088/1674-4926/44/9/090101.
[71] Ge G, Yuan W, Zhao W, Lu Y, Zhang YZ, Wang WJ, Chen P, Huang W, Si WL, Dong XC. Highly stretchable and autonomously healable epidermal sensor based on multi-functional hydrogel frameworks. J Mater Chem A. 2019;7(11):5949. https://doi.org/10.1039/c9ta00641a.
[72] Ma YL, Ouyang JY, Raza T, Li P, Jian AJ, Li ZQ, Liu H, Chen M, Zhang XJ, Qu LJ, Tian MW, Tao GM. Flexible all-textile dual tactile-tension sensors for monitoring athletic motion during taekwondo. Nano Energy. 2021;85:105941. https://doi.org/10.1016/j.nanoen.2021.105941.
[73] Gao W, Emaminejad S, Nyein HYY, Challa S, Chen K, Peck A, Fahad HM, Ota H, Shiraki H, Kiriya D, Lien DH, Brooks GA, Davis RW, Javey A. Fully integrated wearable sensor arrays for multiplexed in situ perspiration analysis. Nature. 2016;529(7587):509. https://doi.org/10.1038/nature16521.
[74] Wang XF, Liu J, Zheng YQ, Shi B, Chen AB, Wang LL, Shen GZ. Biocompatible liquid metal coated stretchable electrospinning film for strain sensors monitoring system. Sci China Mater. 2022;65(8):2235. https://doi.org/10.1007/s40843-022-2081-0.
[75] Ding Y, Jiang J, Wu Y, Zhang Y, Zhou J, Zhang Y, Huang Q, Zheng Z. Porous conductive textiles for wearable electronics. Chem Rev. 2024;124(4):1535. https://doi.org/10.1021/acs.chemrev.3c00507.
[76] Lee GH, Lee YR, Kim H, Kwon DA, Kim H, Yang C, Choi SQ, Park S, Jeong JW, Park S. Rapid meniscus-guided printing of stable semi-solid-state liquid metal microgranular-particle for soft electronics. Nat Commun. 2022;13(1):2643. https://doi.org/10.1038/s41467-022-30427-z.
[77] Cheng W, Wang XY, Xiong Z, Liu J, Liu ZJ, Jin YX, Yao HC, Wong TS, Ho JS, Tee BCK. Frictionless multiphasic interface for near-ideal aero-elastic pressure sensing. Nat Mater. 2023;22(11):1352. https://doi.org/10.1038/s41563-023-01628-8.